

A 95 GHz Methanol Emission Survey Toward Eight Small Supernova Remnants

Yingjie Li^{1,2}, Ye Xu¹, Xi Chen^{3,4}, Deng-Rong Lu¹, Yan Sun¹, Xinyu Du^{1,5} and Zhi-Qiang Shen⁴

¹ Purple Mountain Observatory, Chinese Academy of Sciences, Nanjing 210008, China; xuye@pmo.ac.cn

² University of Science and Technology of China, Chinese Academy of Sciences, Hefei, Anhui 230026, China; liyj@pmo.ac.cn

³ Center for Astrophysics, Guangzhou University, Guangzhou 51006, China; chenxi@shao.ac.cn

⁴ Shanghai Astronomical Observatory, Chinese Academy of Sciences, Shanghai 200030, China

⁵ Graduate University of the Chinese Academy of Sciences, 19A Yuquan Road, Shijingshan District, Beijing 100049, China

Abstract We report on a 95 GHz ($8_0 - 7_1 A^+$) methanol (CH_3OH) emission survey with the Purple Mountain Observatory Delingha 13.7 m telescope. Eight supernova remnants (SNRs) with angular size $\lesssim 10'$ were observed, but emission was only detected in three SNRs near the Galactic center (Sgr A East, G 0.1-0.1, and G 359.92-0.09). CH_3OH emission mainly surrounds the SNRs and can be decomposed into nine spatial peaks with velocity range of eight peaks being $(-30, 70) \text{ km s}^{-1}$, and the other $(70, 120) \text{ km s}^{-1}$. They are probably excited by interaction with these SNRs and adjacent molecular gas in the central molecular zone (CMZ), although star formation may play an important role in exciting CH_3OH emission in some regions of CMZ. We infer that tidal action is unlikely to be an excitation source for CH_3OH emission.

Key words: ISM: molecules – ISM: supernova remnants – Galaxy: center – ISM: kinematics and dynamics – ISM: clouds

1 INTRODUCTION

The methanol molecule (CH_3OH) is a slightly asymmetric top with hindered internal rotation. It processes a multitude of allowed radio transitions. CH_3OH in space has been actively studied since its discovery by Ball et al. (1970), abundant CH_3OH transitions have been detected at sub-millimeter and millimeter wavelengths, and are sensitives to the density and the kinetic temperature of the dense clouds (see e.g., Menten et al., 1988a,b; Leurini et al., 2004, and references therein). CH_3OH is one of the most abundant complex molecules in star formation regions (Kalenskii et al., 1997), where both its thermal (Slysh et al., 1994; Hatchell et al., 1998) and maser (see below) lines can trace star formation activities. However, for CH_3OH lines at 95 GHz ($8_0 - 7_1 A^+$), the attention has mostly been concentrated on its maser (belong to class I CH_3OH maser lines) emission though there are a few detections of thermal emission as well (see e.g., Val'tts et al., 2000; Chen et al., 2012).

Class I CH_3OH maser lines that are pumped by collisions, such as at 36 GHz ($4_{-1} - 3_0 E$), 44 GHz ($7_0 - 6_1 A^+$), 95 GHz ($8_0 - 7_1 A^+$), etc., have long been assumed to be associated with both low-mass and high-mass star formation (Kalenskii et al., 2006; Chen et al., 2011; Yang et al., 2017). From the beginning of 2011, targeted searches for these masers toward supernova remnants (SNRs) had started

Table 1 SNR properties

Name	Interacting with molecular clouds ¹	OH 1720 MHz maser ^a	CH ₃ OH 36/44 GHz maser ^b	Type	X-ray	GeV Flux ^c ($\times 10^{-9}$ ph cm ⁻² s ⁻¹)	TeV ² (σ)
Sgr A East	Y	Y	Y	TC ^d	Y ^e	65.02	HESS(66.6)
G 0.1-0.1	Y?			C? ^f	Y ^g	1.0 ³	HESS (11.5)
G 1.4-0.1	Y	Y	Y	S ^h		0.4 ³	HESS (6.5)
G 29.7-0.3	Y	Y	N	C ⁱ	Y ^j	2.1 ³	HESS (10.1)
G 111.7-2.1	Y?	N		S ^k	Y ^l	6.25	MAGIC (5.2)
G 120.1+1.4	Y?	N		S ^m	Y ^l	2.1 ³	VERITAS (5.8)
G 184.6-5.8	?			F ⁿ	Y ^l	108.12	HESS (129)
G 359.92-0.09 ⁴	Y ^o						

References: (a) Frail et al. (1996); Koralesky et al. (1998); Yusef-Zadeh et al. (1999); Davies et al. (2009); (b) Litovchenko et al. (2011); Pihlström et al. (2011, 2014); (c) Acero et al. (2016); (d) Yusef-Zadeh et al. (2003); Vink (2012); (e) Maeda et al. (2002); (f) Heard & Warwick (2013); (g) Yusef-Zadeh et al. (2002b); (h) Frail (2011); (i) Becker et al. (1983); Blanton & Helfand (1996); (j) Sugizaki et al. (2001); (k) Aharonian et al. (2001); Albert et al. (2007); (l) Predehl & Schmitt (1995); (m) Acciari et al. (2011); (n) Wallace et al. (1994, 1999); (o) Coil & Ho (2000); Herrnstein & Ho (2005); Amo-Baladrón et al. (2011).

Notes: In the column of “Type”, S=shell, C=composite, F=plerion, TC=thermal composite (i.e. mixed-morphology), C?=probably thermal & plerionic composite. In the other columns, Y=yes, N=no, Y?=probable, ?=possible, Null=no data.

(1) see “A List of Galactic SNRs Interacting with Molecular Clouds”, and references therein (<http://astronomy.nyu.edu.cn/~ygchen/others/bjiang/interSNR6.htm>).

(2) This column includes TeV γ -ray detections by experiment and significance of detection in parentheses for HESS (Aharonian et al., 2006, 2008; Bochow, 2011), MAGIC (Albert et al., 2007) and VERITAS (Acciari et al., 2011).

(3) Upper limits of flux with 99% confidence and PL index $\Gamma = 2$, see Table 3 in Acero et al. (2016).

(4) This SNR is included neither in “A census for high-energy-observations of Galactic supernova remnants” (<http://www.physics.umanitoba.ca/snr/SNRcat/>, Ferrand & Safi-Harb, 2012) nor in “A catalogue of Galactic supernova remnants” (<http://www.mrao.cam.ac.uk/surveys/snr/s/>, Green, 2014).

carrying out (Litovchenko et al., 2011). These maser emission, such as at 36 GHz ($4_{-1} - 3_0$ E) and 44 GHz ($7_0 - 6_1$ A⁺), has been detected in some supernova remnants (SNRs) (Litovchenko et al., 2011; Pihlström et al., 2011, 2014). However, there is only one detection of 95 GHz CH₃OH maser line in SNRs (i.e., SNR Kes 79, Zubrin & Shulga, 2008), and it is controversial in that Frail (2011) claimed that the 12 m Arizona Radio Observatory failed to confirm this detection. The CH₃OH maser line at 95 GHz is excited under a stricter range of conditions than that at 36 and 44 GHz (see e.g., McEwen et al., 2014; Nesterenok, 2016). That may be the factor that fewer 95 GHz CH₃OH maser emission was detected in SNRs. The factor may also be an effect of not having a large survey of SNRs at 95 GHz. We interest in whether CH₃OH emission is associated with SNRs.

Yusef-Zadeh et al. (2013) explained the enhanced abundance of CH₃OH in the Galactic center in terms of the interaction between cosmic rays and molecular gas, which produces γ -rays (Frail, 2011). Therefore, the presence of γ -ray emission such as at GeV or TeV energies marks a possibility of enhanced abundance of CH₃OH (such as at 36, 44 and 95 GHz), and hence may raise the possibility of detection. Although the excitation conditions for these three masers are different, all three maser emission outputs are presented over a wide range of environments (see e.g., McEwen et al., 2014; Leurini et al., 2016). In order to expect a high detection rate and save time, the selection criteria were that the SNRs were small ($\lesssim 10'$) and associated with class I methanol 36/44 GHz maser or GeV/TeV emission. We selected eight SNRs, with three (Sgr A East, G 0.1-0.1, and G 359.92-0.09) located in the Galactic center. Table 1 summarizes the physical properties of the selected SNRs, including their interaction with clouds, occurrence of 1720 MHz OH and class I methanol 36/44 GHz maser, SNR type, and high-energy emission.

We report on a 95 GHz CH₃OH emission survey toward eight SNRs using the Purple Mountain Observatory Delingha (PMODLH) 13.7 m radio telescope. Observation and data reduction are described in Section 2, and the survey outcomes in Section 3. Section 4 discusses whether the 95 GHz CH₃OH emission can be identified as maser lines. In section 5, we discuss the correlation of 95 GHz CH₃OH emission with SNRs, star formation and tidal action, and why 95 GHz CH₃OH emission was only detected around Sgr A East, G 0.1-0.1 and G 359.92-0.09. Finally, Section 6 summarizes the important results.

2 OBSERVATION AND DATA REDUCTION

Using the Purple Mountain Observatory Delingha (PMDLH) 13.7 m telescope, CH_3OH (8_0-7_1 A^+ , 95.16949 GHz, hereafter 95 GHz CH_3OH) line was observed toward eight SNRs from May 5 to June 25, 2015. The telescope operates in sideband separation mode, and uses a fast Fourier transform spectrometer (Shan, Yang & Shi, 2012).

Sgr A East, G 0.1-0.1 and G 359.92-0.04 were mapped in a single image spanning $\sim 20' \times 20'$ (49.5 pc^2 at 8.5 kpc) cell (denote this region as Galactic central SNRs region, GCSNRR), and the remaining five SNRs were mapped in $10' \times 10'$ cells (see Table 2). We used the on-the-fly (OTF) observational mode with a constant rate of $50'' \text{ s}^{-1}$ along lines in R.A. and Decl. directions on the sky. The receiver recorded spectra every 0.3 s. The standard chopper wheel method was used for calibration (Penzias & Burrus, 1973; Ulich & Haas, 1976). The half-power beam width of the telescope was approximately $58''$ at 95 GHz. Typical system temperature, T_{sys} , during the observations was 160–190 K. Antenna temperatures, T_{A}^* , were calibrated to the main beam temperatures, T_{R}^* , with main beam efficiency $\eta_{\text{mb}} = 62\%$. The calibrated data were re-gridded to $30''$ pixels. Table 2 summarizes mapping center and main beam root mean square noise (RMS) per 61 kHz channel (corresponding to 0.19 km s^{-1} at 95 GHz) for each target source.

Table 2 Observed SNRs Positions and Observing RMS

Region	R.A. (J2000)	Decl. (J2000)	Size (arcmin)	RMS (mK)
GCSNRR ¹	17 45 44.0	-29 00 00	20	25
G 1.4-0.1	17 49 39.0	-27 46 00	10	25
G 29.7-0.3	18 46 25.0	-02 59 00	10	39
G 111.7-2.1	23 23 26.0	58 48 00	10	28
G 120.1+1.4	00 25 18.0	64 09 00	10	29
G 184.6-5.8	05 34 31.0	22 01 00	10	27

Notes: The columns show the name, mapping center in equatorial coordinates (J2000), mapping size and RMS per channel of each region.

(1) This region covers SNRs Sgr A East, G 0.1-0.1 and G 359.92-0.09.

3 RESULTS

The survey resulted in three detections (Sgr A East, G 0.1-0.1 and G 359.92-0.09) that are covered by GCSNRR. We focused on the general distribution of 95 GHz CH_3OH emission in GCSNRR in this section.

Figure 1 shows 95 GHz CH_3OH integrated intensity map, where Sgr A* is indicated by a blue filled pentagram. The 95 GHz CH_3OH emission south of Decl. $\sim -29^\circ 02'$ shows two distinct velocity components. We integrated the emission separately over the low velocity component, -30 to 70 km s^{-1} (Figure 1, the left panel), and high velocity component, 70 to 120 km s^{-1} (Figure 1, the right panel).

Nine spatial peaks were evident, shown in Figure 1 by diamonds, and listed in Table 3. Only one position, located in the southwestern region of the map, contains two peaks, corresponding to peak 8 for the low velocity gas (Figure 1, the left panel) and peak 9 for the high velocity (Figure 1, the right panel). Peak 9, where velocity is centered at $\sim 85 \text{ km s}^{-1}$, is much weaker with integral intensity of 0.47 K km s^{-1} . Figure 1 also indicates that most 95 GHz CH_3OH emission surrounds SNRs. The correlation between them would be discussed in section 5.1.

Figure 2 presents the spectra of the nine emission peaks. The spectrum of peak 4 shows a bimodal structure. For peak 5, the spectrum shows a possible second velocity component centered at $\sim 45 \text{ km s}^{-1}$, where the peak T_{R}^* of this component is less than $3 \times \text{RMS}$. The spectrum of peak 7 indicates a second velocity component centered at $\sim 85 \text{ km s}^{-1}$, which surrounds peak 9 from spatial distribution (see the right panel of Figure 1). The spectra of the remaining peaks are centrally dominated.

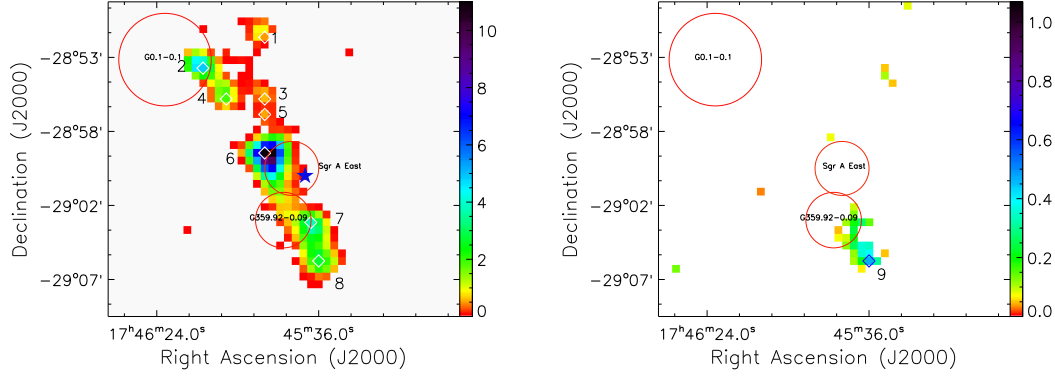


Fig. 1 Integrated intensity maps of 95 GHz CH_3OH , integrated over -30 to 70 km s^{-1} (left), and 70 to 120 km s^{-1} (right), respectively. Color bars units are K km s^{-1} . Maximum integral intensity of 95 GHz CH_3OH in the left and right panels are 10.94 and 0.47 K km s^{-1} , and the scales are 11.0 and 1.1 K km s^{-1} , respectively. The blue filled pentagram indicates the position of Sgr A*. The diamonds show peak positions. The red circles indicate SNRs. The circles indicating G 359.92-0.09 and Sgr A East are the real angular size. The size of SNR G 0.1-0.1 is uncertain.

Table 3 Peak Emission for 95 GHz CH_3OH

Peak ID	R.A. (J2000)	Decl. (J2000)	Velocity (km s^{-1})	Integrated intensity (K km s^{-1})
peak 1	17:45:52.0	-28:51:30	49.9	0.92
peak 2	17:46:10.3	-28:53:30	53.0	4.80
peak 3	17:45:52.0	-28:55:30	46.7	0.59
peak 4	17:46:03.4	-28:55:30	47.0	1.93
peak 5	17:45:52.0	-28:56:30	-6.4	0.52
peak 6	17:45:52.0	-28:59:00	43.2	10.94
peak 7	17:45:38.3	-29:03:30	18.8	3.73
peak 8	17:45:36.0	-29:06:00	6.8	2.65
peak 9	17:45:36.0	-29:06:00	84.8	0.47

Notes: The fourth column is the intensity weighted velocity (moment 1). The last column is integrated intensity which integrated over velocity from -30 to 70 km s^{-1} for peaks 1-8, and from 70 to 120 km s^{-1} for peak 9.

Figure 3 shows the velocity (intensity weighted, i.e., moment 1) structure of the entire region for both the low (the left panel) and high velocity component (the right panel). A significant velocity gradient from the southwest to northeast is evident in both panels. Velocities for the low velocity component (the left panel) vary from ~ 10 to $\sim 60 \text{ km s}^{-1}$, and from ~ 80 to $\sim 100 \text{ km s}^{-1}$ for the high velocity component (the right panel).

Figure 4 shows the position-velocity map along the black arrow marked in Figure 3. The peak emission is centered at $\sim 45 \text{ km s}^{-1}$. There is also a variation of velocities from ~ 10 to $\sim 60 \text{ km s}^{-1}$ from the southwest to northeast, with corresponding velocity gradient $\sim 2 \text{ km s}^{-1} \text{ pc}^{-1}$. The velocity gradient decreases when the position passes $\sim 0^\circ.20$. There is a similar velocity gradient for the high velocity component (position ranges from $\sim 0^\circ.02$ to $0^\circ.12$), but the emission is much weaker.

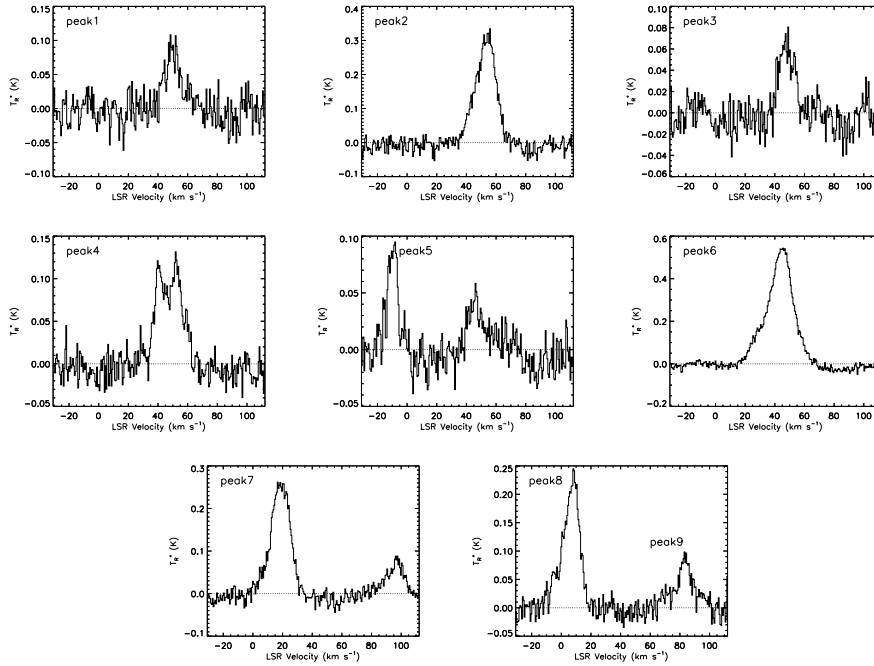


Fig. 2 Spectra of peaks from Table 3. Spectra are averaged over three velocity channels.

4 IS 95 GHz CH₃OH EMISSION MASER EMISSION?

Similar to previous work toward the vicinities of Sgr A and Sgr B2 (Val'tts et al., 2000), the broad line profiles in Figure 2 suggest that thermal emission contributes significantly to the detections.

The distribution of 95 GHz CH₃OH emission is concentrated. In order to avoid the emission peaks being divided by pixels, the central zone is assumed to contain four pixels, i.e., 1' square. The central zone peak intensity is much higher than the pixels outside it. For peaks 1–5, integrated intensities outside the central zone are $\lesssim 60\%$ of the central zone peak intensity. This implies that peak intensities arise from compact areas, i.e., the emission has limited spatial extent, which indicates that maser emission may make a contribution to the total 95 GHz CH₃OH emission in peaks 1–5.

The 95 GHz CH₃OH maser originates in the same clump of gas that produces the 36 and 44 GHz CH₃OH maser (Plambeck & Menten, 1990). Figure 5 indicates that the 95 GHz CH₃OH emission correlates with the 36/44 GHz CH₃OH maser emission in some regions, and most of those co-location regions are around or in peaks 6 – 8. This also indicates that part of 95 GHz CH₃OH emission may be maser emission, particularly in regions around or in peaks 6 – 8. The velocities of 36/44 GHz CH₃OH masers in Figure 5 are less than 60 km s⁻¹, so we did not compare these with the high velocity component of 95 GHz CH₃OH emission.

Thus, there may be a small fraction of 95 GHz CH₃OH maser emission buried within thermal emission, and higher resolution and sensitivity observations would help to confirm this speculation.

5 EXCITATION SOURCE FOR 95 GHz CH₃OH EMISSION

In this section, we extended peaks to clouds that were distinguishable from each other and clearly covered the corresponding peaks, and numbered clouds accordingly (e.g., cloud 1 corresponds to peak 1). We discussed the possible excitation sources for 95 GHz CH₃OH emission. Surveys have revealed

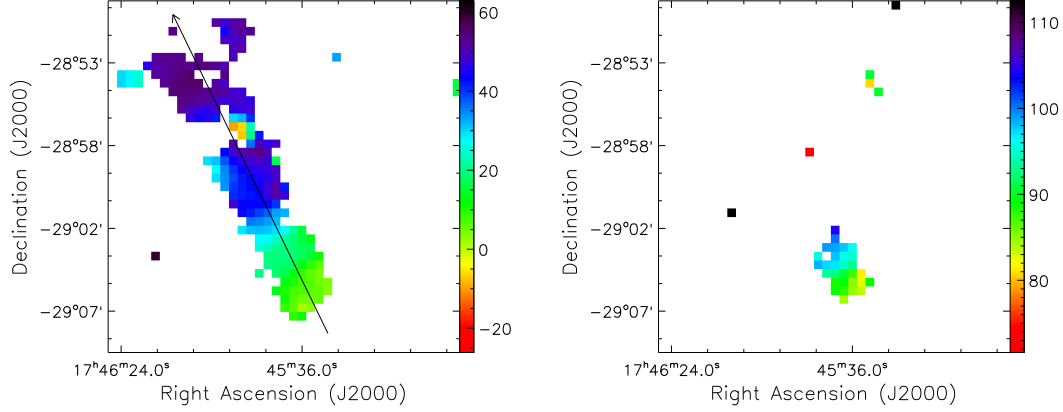


Fig. 3 Velocity maps of 95 GHz CH_3OH . Color bar units are km s^{-1} . Color images show the intensity weighted velocity (moment 1), V_{LSR} , distribution of 95 GHz CH_3OH . The left and right panels show the velocity distribution of low ($-30, 70$) km s^{-1} and high ($70, 120$) km s^{-1} velocity components, respectively. The scales of the left and right panels are ($-30, 70$) and ($70, 120$) km s^{-1} , respectively. The long black arrow in the left panel indicates the axis of the position-velocity map shown in Figure 4.

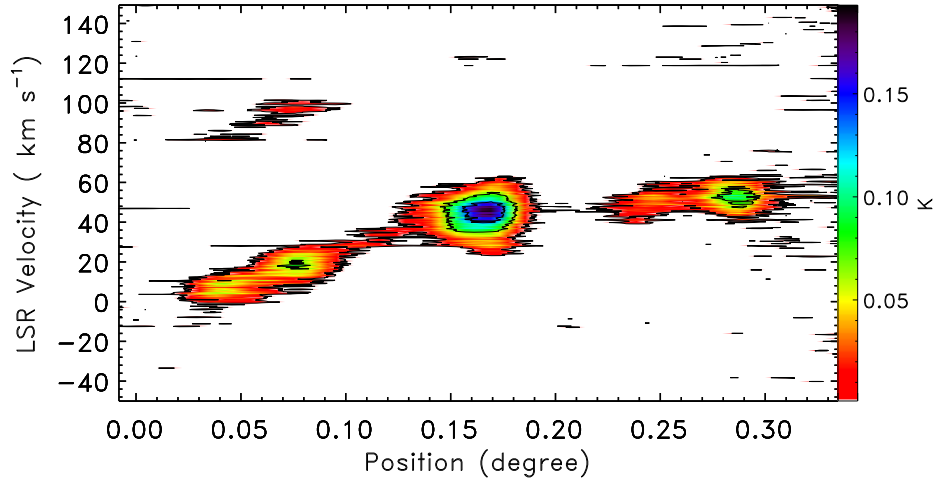


Fig. 4 Position-velocity map of 95 GHz CH_3OH along the arrow shown in Figure 3. Spectra at each position were averaged over $5'$ perpendicular to the axis. $0^{\circ}.00$ on the x-axis corresponds to (R.A., Decl.)=($17^{\text{h}}45^{\text{m}}29.1^{\text{s}}$, $-29^{\circ}08'30''$); and $0^{\circ}.34$ to (R.A., Decl.)=($17^{\text{h}}46^{\text{m}}10.3^{\text{s}}$, $-28^{\circ}50'00''$). Contour levels are 15%, 45%, and 75% of the maximum value (0.19 K).

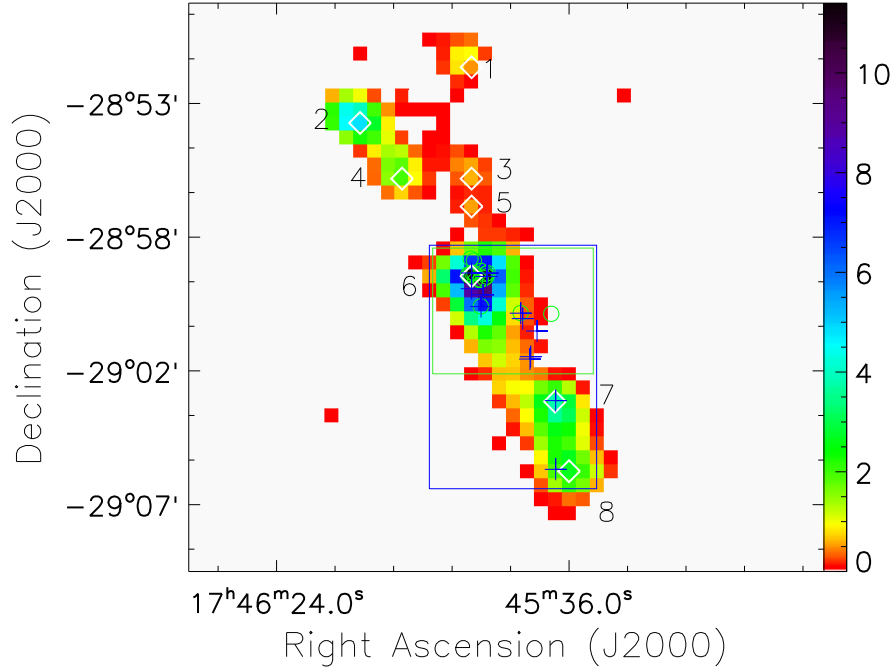


Fig. 5 Relative positions of the 36 GHz CH_3OH masers (blue pluses; Liechi & Wilson, 1996; Sjouwerman et al., 2010, and references therein), 44 GHz CH_3OH masers (green open circles; Pihlström et al., 2011, and references therein), and 95 GHz CH_3OH emission (color image, integrated over -30 to 70 km s^{-1} , the scale is 10.6 K km^{-1}). Color bar units are K km s^{-1} . The blue and green rectangles indicate the study regions of 36 and 44 GHz CH_3OH masers in those references, respectively.

that class I methanol masers, such as 36 and 44 GHz methanol masers, are associated with not only star formation (Kalenskii et al., 2010; Chen et al., 2012), but also SNRs (Litovchenko et al., 2011; Pihlström et al., 2011, 2014). To investigate which one dominates the excitation for 95 GHz CH_3OH emission in GCSNRR, we combined data of 20 cm continuum emission, 36 GHz CH_3OH and 1720 MHz OH maser emission, HII regions, and WISE data. We also discussed the influence of tidal action, because GCSNRR is close to the Galactic center. We also discussed why 95 GHz CH_3OH emission was only detected in GCSNRR. A summary was given in the end of this section.

5.1 Interaction between 95 GHz CH₃OH Emission and SNRs

5.1.1 Relative Position among 95 GHz CH₃OH Emission and SNRs or Superbubble

The 5 GHz and 20 cm continuum emission can trace both HII regions and SNRs in the vicinity of Sgr A East (Serabyn et al., 1992; Yusef-Zadeh et al., 2004). For example, there are distinct differences in the 20 cm continuum emission map between HII regions (Yusef-Zadeh et al., 2004, Figure 19b, 21a and 23b) and SNRs (Yusef-Zadeh et al., 2004, Figure 19b and 21a). We used the 20 cm continuum emission map to indicate SNRs. Figure 6 shows the 95 GHz CH₃OH emission contours superimposed on the 20 cm radio continuum emission image from Yusef-Zadeh et al. (2004). To show the 20 cm radio continuum emission more explicitly, the two images have different maximal values: the left panel = 4.5 Jy beam⁻¹ and the right panel = 1.0 Jy beam⁻¹.

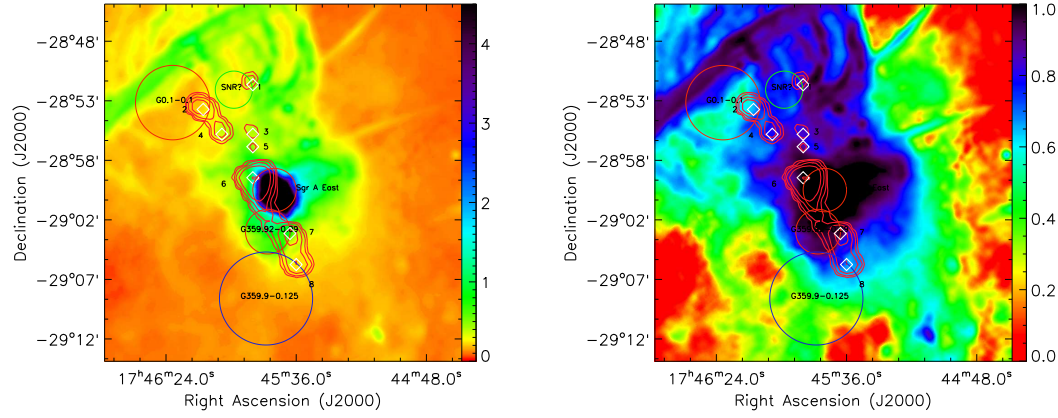


Fig. 6 Contours of 95 GHz CH₃OH emission between -30 and 70 km s⁻¹ superimposed on the 20 cm radio continuum image from Yusef-Zadeh et al. (2004). Contours start at 3σ and increase in steps of 1, 2, 4, 8, and $16\times 3\sigma$, where $\sigma = 0.11$ K km s⁻¹. Color bars units are Jy beam⁻¹, and the scales of the left and right panels are 4.5 and 1.0 Jy beam⁻¹, respectively. The red circles indicate SNRs, the green circle indicates an SNR candidate (marked as “SNR?”), and the blue circle indicates a superbubble candidate. The circles indicating G 359.92-0.09 and Sgr A East are the real angular size, and that of G 359.9-0.125 is half the real angular size. The sizes of SNR G 0.1-0.1 and “SNR?” are uncertain. The diamonds indicate peak positions, and contours outline clouds.

The blue circle in figure 6 indicates a superbubble candidate, G 359.9-0.125, centered at $(l, b) \sim (359.84^\circ, -0.14^\circ)$ with size $15' \times 3'$ (Mori et al., 2008; Ponti et al., 2015, and references therein). The red circles indicate three SNRs: Sgr A East, G 0.1-0.1 and G 359.92-0.09. SNRs Sgr A East is clear in the left panel, and the right panel probably shows a shell-like structure in the vicinity of cloud 1. This shell-like structure may indicate an SNR candidate located at R.A. $\sim 17^{\text{h}}46^{\text{m}}00^{\text{s}}$, Decl. $\sim -28^\circ52'12''$; and represented by a green circle marked with “SNR?”.

Cloud 1 lies in the northwest of the SNR candidate. Clouds 2 and 4 are in the southwest of the SNR G 0.1-0.1 and located in molecular cloud G 0.13-0.13. They are probably interacting with G 0.1-0.1 just as G 0.13-0.13 doing (Yusef-Zadeh et al., 2002a). The ridge connecting clouds 6, 7 and 8 (i.e.,

Mol. Ridge or Molecular Ridge in Herrnstein & Ho, 2005; Amo-Baladrón et al., 2011) surrounds the eastern edge of Sgr A East. SNR G 359.92-0.09, which is located to the east of them, probably has a strong interaction with Sgr A East and the eastern edge of the 20 km s^{-1} cloud (Coil & Ho, 2000; Herrnstein & Ho, 2005; Amo-Baladrón et al., 2011), where clouds 7 and 8 are located. The southeast of clouds 8 and 9 (the position of peak 9 overlaps with peak 8, see figure 1) may interact with superbubble candidate G 359.9-0.125, as shown in Figure 6. Most of the 95 GHz CH_3OH emission surround SNRs (Figure 6), which suggests that the emission may be excited by interaction with SNRs.

5.1.2 Line Widths of 95 GHz CH_3OH Emission Versus SNRs or Superbubble

Molecular line widths can be broadened by interaction between shock and molecular cloud (Kilpatrick et al., 2014). Furthermore, line broadenings were regarded as strong kinematic evidence for the interaction between SNR and molecular cloud (Jiang et al., 2010; Kilpatrick et al., 2016, and references therein). For instance, the broad CS (1-0) line widths were used to indicate the interaction between the Sgr A East shell and the 50 km s^{-1} molecular cloud (Tsuboi et al., 2009). Therefore, 95 GHz CH_3OH line width broadening may be an indicator of interaction among SNRs and 95 GHz CH_3OH clouds. Figure 7 shows the distribution of line widths for 95 GHz CH_3OH emission. The line for the high velocity component is randomly distributed in the region around peak 9, and therefore omitted in Figure 7.

Figure 7 shows four interesting regions marked by rectangles:

Region A. Line widths relatively higher than their neighborhoods show a reversed-S structure crossing the interface between clouds 7 and 8. In this region, the north part of the reversed-S structure is located west of cloud 7, possibly indicating an interaction among cloud 7, SNR G 359.92-0.09, and Sgr A East. The midsection of the reversed-S structure may indicate SNR G 359.92-0.09 rushing toward cloud 8, or may trace an interaction between clouds 7 and 8. The south part of the reversed-S structure lies south of cloud 8, which may indicate an interaction between cloud 8 and superbubble candidate G 359.9-0.125.

Region B. Line widths in cloud 6 (typical value is $\sim 20 \text{ km s}^{-1}$) are much higher than in other regions, and increase toward the east. This possibly indicates that the 50 km s^{-1} cloud (including cloud 6) has a strong interaction with Sgr A East.

Region C. Line widths increase toward the southeast of cloud 4 and west of cloud 2, which constitutes a faint shell. This may suggest an interaction between the 95 GHz CH_3OH cloud and SNR G 0.1-0.1.

Region D. Line widths are higher in the northeast of cloud 1, which may indicate that cloud 1 is interacting with an SNR candidate as discussed above to the east of cloud 1 (see the green circle in the right panel of Figure 6 and Figure 7). This emission may be also excited by star formation as discussed in Section 5.2.

Figure 7 also shows that 95 GHz CH_3OH line widths are associated with the 36 GHz CH_3OH masers in the south of Decl. $\sim -28^\circ 58'$ and 1720 MHz OH masers around Sgr A East. The geometry of the 36 GHz masers in Sgr A East outlines the current location of an SNR shock front (Sjouwerman & Pihlström, 2012). Most 1720 MHz OH masers arise in regions where the SNR Sgr A East is interacting with the 20 and 50 km s^{-1} molecular clouds and the nearby SNR G 359.92-0.09 (Sjouwerman & Pihlström, 2008). The 50 km s^{-1} molecular cloud includes cloud 6, and the 20 km s^{-1} molecular cloud includes clouds 7 and 8.

As a summary of this subsection, 95 GHz CH_3OH emission may be excited by interaction with SNRs and its line width is probably a good tracer of SNRs.

5.2 Effect of Star Formation

The 95 GHz CH_3OH emission has usually assumed to be associated with star formation (Chen et al., 2011; Yang et al., 2017). HII regions and WISE data were used to indicate star formation regions in this study. Figure 8 superimposes the positions of HII regions (yellow crosses, abstracted from Goss et al.,

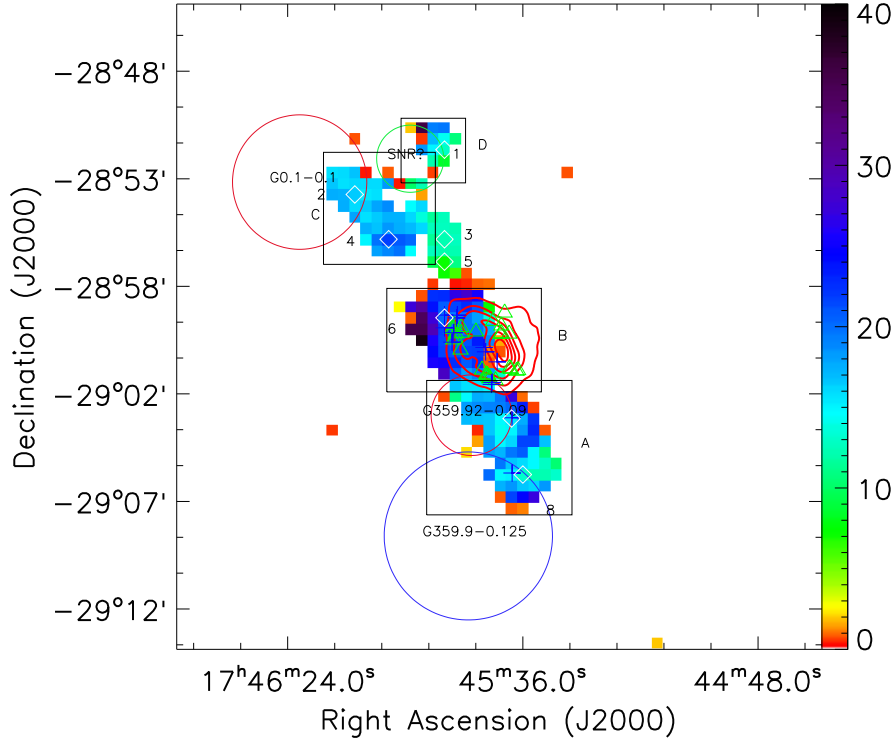


Fig. 7 Distribution of 95 GHz CH_3OH line widths (color image). Maximum is 38.54 km s^{-1} . Color bar units are km s^{-1} . Red contours of the 20 cm continuum image (Yusef-Zadeh et al., 2004) show Sgr A East. The lowest contour level and contour interval are 15% of the maximum ($11.23 \text{ Jy beam}^{-1}$). Green triangles indicate 1720 MHz OH masers (see Sjouwerman & Pihlström, 2008, and references therein), and blue pluses indicate 36 GHz CH_3OH masers (Liechti & Wilson, 1996; Sjouwerman et al., 2010, and references therein). The four rectangles present four interesting regions.

1985; Kuchar & Clark, 1997; Paladini et al., 2003; Anderson et al., 2014, and reference therein) on the WISE false color map, along with the 95 GHz CH_3OH emission contours. Both the HII regions and the WISE emission show that 95 GHz CH_3OH emission deviates slightly from the star formation regions.

The region, where star formation is most likely to be the dominant excitation source for 95 GHz CH_3OH emission in GCSNRR, is cloud 1, because the nearest HII region lies just $0.40'$ west of peak 1. The WISE emission also shows that star formation is probably play an important role in exciting CH_3OH emission in clouds 2 – 5.

Star formation may not be the dominant factor to excite 95 GHz CH_3OH emission in the 50 km s^{-1} cloud (including cloud 6), because the energy restored in star formation process may be less than the kinetic energy in 50 km s^{-1} cloud. Specifically, the energy restored in protostellar outflows is up to $10^{47} - 10^{48} \text{ erg}$ (Bachiller, 1996; Livio, 2000). That is far less than the kinetic energy in the 50 km s^{-1} cloud ($0.5m \cdot \Delta V^2 \sim 10^{50} \text{ erg}$), where its mass, m , is $\sim 5 \times 10^4 M_{\odot}$ (Herrnstein & Ho, 2005) and line width, ΔV , in terms of $\text{CH}_3\text{OH} \sim 20 \text{ km s}^{-1}$ (no less than 10 km s^{-1}). Therefore, SNR Sgr A East is

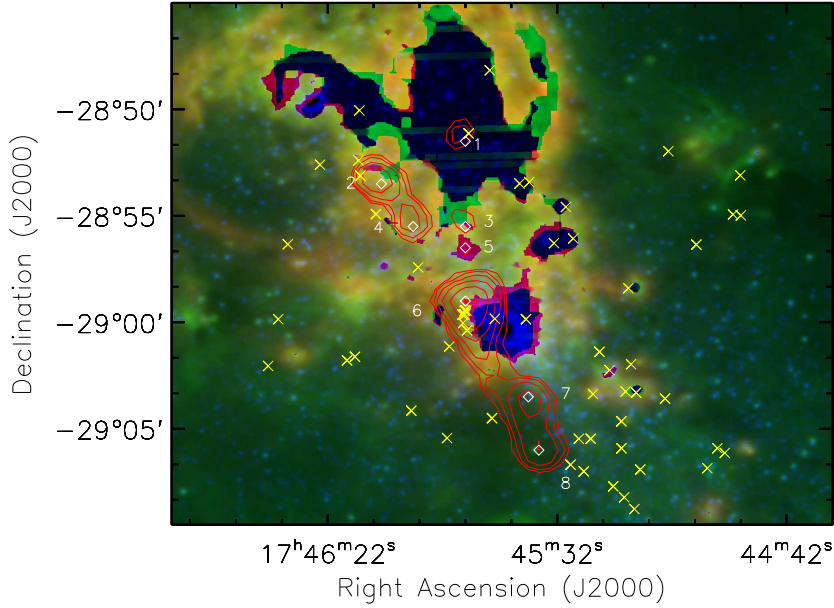


Fig. 8 Background false color map, where blue is the WISE 4.6 μm , green is 12 μm , and red is 22 μm data, with 95 GHz CH_3OH emission contours between -30 and 70 km s^{-1} and HII regions superimposed (yellow crosses, abstracted from Goss et al., 1985; Kuchar & Clark, 1997; Paladini et al., 2003; Anderson et al., 2014, and references therein). Contours start at 3σ and increase in steps of 1, 2, 4, 8, and $16 \times 3\sigma$, where $\sigma = 0.11 \text{ K km s}^{-1}$. The diamonds indicate peak positions, and contours outline clouds.

more likely to be the dominant excitation source than star formation in the 50 km s^{-1} cloud (including cloud 6).

In clouds 7–9, both HII regions and WISE emission deviate from 95 GHz CH_3OH emission, which suggests that the star formation action is probably not the dominant excitation source in clouds 7–9.

5.3 Influence of Tidal Action

The Roche density n_{RL} is given by (Mapelli & Gualandris, 2016):

$$n_{\text{RL}} \sim 10^7 \text{ cm}^{-3} \left(\frac{m_{\text{BH}}}{3 \times 10^6 M_{\odot}} \right) \left(\frac{\text{pc}}{r} \right)^3, \quad (1)$$

where $m_{\text{BH}} = 4.30 \pm 0.20_{\text{stat}} \pm 0.30_{\text{sys}} \times 10^6 M_{\odot}$ is the mass of the supermassive black hole (Gillessen et al., 2009; Mapelli & Gualandris, 2016), and r is the distance of the molecular cloud from the supermassive black hole. Clouds 6–8 are located in the 20 or 50 km s^{-1} clouds, which are ~ 20 pc from the supermassive black hole Sgr A* (Mapelli & Gualandris, 2016). Then n_{RL} is no less than $1.8 \times 10^6 \text{ cm}^{-3}$, which is much higher than the number densities in 20 and 50 km s^{-1} clouds ($0.4 - 4 \times 10^5 \text{ cm}^{-3}$, see Table 3 of Amo-Baladr3n et al., 2011). This indicates that the 20 and 50 km s^{-1}

clouds are currently being tidally disrupted according to Mapelli & Gualandris (2016), which is also suggested by Herrnstein & Ho (2005).

Assuming near equatorial and near-circular orbit about Sgr A*, the tidal potential, V_{tidal} , can be estimated as (Murray & Dermott, 2000)

$$V_{\text{tidal}} = \frac{Gm_{\text{BH}}}{4a^3} R^2 (3 \cos \psi + 1), \quad (2)$$

where a and R are the distance of the 50 km s^{-1} cloud from the black hole, and the radius of the black hole, respectively, and ψ is the angle between the projected radius vector and the plane perpendicular to the link line between the center of the 50 km s^{-1} cloud and the black hole. Even if $a = R = 0.04 \text{ pc}$, where 0.04 pc is the upper limit of the radius of the black hole (Amo-Baladrón et al., 2011), $V_{\text{tidal}} \sim 10^{18} \text{ erg}$, which is far less than the kinetic energy in 50 km s^{-1} cloud (i.e., $\sim 10^{50} \text{ erg}$, see section 5.2). That indicates that tidal action is not likely to be a source to excite CH_3OH emission, although the estimate above is quite approximate. Similar conclusion applies to the 20 km s^{-1} cloud.

5.4 The Role of Cosmic Rays

Observing 36 GHz CH_3OH in CMZ (covers GCSNRR), Yusef-Zadeh et al. (2013) explained the enhanced abundance of CH_3OH in terms of interactions between cosmic rays and molecular gas. Since 95 GHz CH_3OH emission is associated with 36 GHz CH_3OH emission (see Figure 5 and Figure 7), the 95 GHz CH_3OH emission can be enhanced by these interactions in CMZ.

5.5 The Possible Reason Why 95 GHz CH_3OH Emission Was Only Detected in GCSNRR

Table 1 lists the properties of the eight SNRs, and in particular indicates that the type of SNRs is the unique character of SNRs Sgr A East and G 0.1-0.1 with the detection of 95 GHz CH_3OH emission. SNR G 0.1-0.1 and Sgr A East are probably thermal & plerionic composite (Heard & Warwick, 2013) and thermal composite (Yusef-Zadeh et al., 2003; Vink, 2012) SNRs, respectively.

Thermal composite SNRs have interior thermal X-ray emission, and are also known as mixed morphology SNRs (MM SNRs). Frail et al. (1996) and Green et al. (1997) first noted that the OH (1720 MHz) SNRs (SNRs that have detected 1720 MHz OH masers) belonged predominantly to a particular class of MM SNRs that have center-filled thermal X-ray emission. This hypothesis was verified on a firmer statistical footing by Yusef-Zadeh et al. (2003). Interactions between SNR and molecular cloud play an important role in producing this interior X-ray gas (Frail, 2011). The 95 GHz CH_3OH emission in cloud 6 is associated with 1720 MHz OH maser emission, which also supports a possible correlation between SNR type and 95 GHz CH_3OH emission. This correlation could also be one of the possible reasons why 95 GHz CH_3OH emission was only detected in GCSNRR.

On the other side, interaction between cosmic rays and molecular gas may be another reason why 95 GHz CH_3OH emission was only detected in GCSNRR. Cosmic rays collide with ambient gas produce γ -rays (Frail, 2011), such as GeV/TeV emission. The region surrounding the Galactic center is among the brightest and most complex in high-energy γ -rays (Ajello et al., 2016, and references therein). Although both the GeV and TeV fluxes around Sgr A East are less than that in G 184.6-5.8, they are much higher than that in G 1.4-0.1, G 29.7-0.3, G 111.7-2.1 and G 120.1+1.4 (see Table 1). In addition, it is unlikely that SNR G 184.6-5.8 interacts with molecular clouds (Graham et al., 1990; Fish et al., 2007; Kilpatrick et al., 2016). Therefore, the interaction between cosmic rays and molecular gas near the Galactic center could still be one of the possible reasons why 95 GHz CH_3OH emission was only detected in GCSNRR.

As a summary of this section, 95 GHz CH_3OH emission is probably excited by interaction with SNRs and may also correlate with the type of SNRs. Although star formation may play an important role in exciting CH_3OH emission 95 GHz CH_3OH emission in some regions, it is probably not the dominant excitation source in clouds 7 – 9, and may not be the dominant excitation source in cloud 6. It is difficult to clarify whether star formation or SNRs is the dominant excitation source in clouds 1

– 5. Interaction between cosmic rays and molecular gas in CMZ may enhance 95 GHz CH₃OH emission. The contribution from tidal action to exciting 95 GHz CH₃OH emission is negligible. We also suggest that the possible reasons why 95 GHz CH₃OH emission was only detected in GCSNRR may be correlated with the type of SNRs near the Galactic center, and the interaction between cosmic rays and molecular gas in CMZ. However, a larger sample in the future survey is required to confirm the correlation between 95 GHz CH₃OH emission and the type of SNRs.

6 SUMMARY

We conducted a survey for 95 GHz ($8_0 - 7_1 A^+$) CH₃OH emission toward eight SNRs with angular size $\lesssim 10'$. The main summaries are as follows:

1. 95 GHz CH₃OH emission was only detected in Sgr A East, G 0.1-0.1 and G 359.92-0.09. The emission can be decomposed into nine spatial peaks with velocity range of eight peaks being (-30, 70) km s⁻¹, and the other (70, 120) km s⁻¹.
2. Part of the 95 GHz CH₃OH emission may be maser emission in some regions, particularly in regions around or in peaks 1 – 8. Higher resolution and sensitivity observations are required to confirm this speculation.
3. Most 95 GHz CH₃OH emission surrounds SNRs, and is probably excited by interacting with SNRs in CMZ, although star formation is probably important to excite 95 GHz CH₃OH emission in some regions of CMZ. The influence of tidal action is negligible.
4. SNR type and interaction between cosmic rays and molecular gas in CMZ could be possible reasons why 95 GHz CH₃OH emission was only detected toward SNRs near the Galactic center. A larger sample is required to confirm the correlation between 95 GHz CH₃OH emission and the type of SNRs.

Acknowledgements We acknowledge Fa-cheng Li, Yuliang Xin, Zhaoqiang Shen and Yuehui Ma for their valuable help, and thank Farhad Yusef-Zadeh for providing 20 cm radio image. This work was supported by the National Science Foundation of China (Grant Numbers: 11673066, 11233007, 11590781 and 11273043), and the Key Laboratory for Radio Astronomy.

References

- Acciari, V. A., Aliu, E., Arlen, T., et al. 2011, *ApJ*, 730, L20
 Acero, F., Ackermann, M., Ajello, M., et al. 2016, *ApJS*, 224, 8
 Aharonian, F., Akhperjanian, A., Barrio, J., et al. 2001, *A&A*, 370, 112
 Aharonian, F., Akhperjanian, A. G., Barres de Almeida, U., et al. 2008, *A&A*, 488, 219
 Aharonian, F., Akhperjanian, A. G., Bazer-Bachi, A. R., et al. 2006, *A&A*, 457, 899
 Ajello, M., Albert, A., Atwood, W. B., et al. 2016, *ApJ*, 819, 44
 Albert, J., Aliu, E., Anderhub, H., et al. 2007, *A&A*, 474, 937
 Amo-Baladrón, M. A., Martín-Pintado, J., & Martín, S. 2011, *A&A*, 526, A54
 Anderson, L. D., Bania, T. M., Barger, D. S., et al. 2014, *ApJS*, 212, 1
 Bachiller, R. 1996, *ARA&A*, 34, 111
 Ball, J. A., Gottlieb, C. A., Lilley, A. E., & Radford, H. E. 1970, *ApJ*, 162, L203
 Becker, R. H., Helfand, D. J., & Szymkowiak, A. E. 1983, *ApJ*, 268, L93
 Blanton, E. L., & Helfand, D. J. 1996, *ApJ*, 470, 961
 Bochow, A. 2011, Ph.D. Thesis,
 Chen, X., Ellingsen, S. P., He, J.-H., et al. 2012, *ApJS*, 200, 5
 Chen, X., Ellingsen, S. P., Shen, Z.-Q., Titmarsh, A., & Gan, C.-G. 2011, *ApJS*, 196, 9
 Coil, A. L., & Ho, P. T. P. 2000, *ApJ*, 533, 245
 Davies, B., Origlia, L., Kudritzki, R.-P., et al. 2009, *ApJ*, 694, 46
 Ferrand, G., & Safi-Harb, S. 2012, *Advances in Space Research*, 49, 1313
 Fish, V. L., Sjouwerman, L. O., & Pihlström, Y. M. 2007, *ApJ*, 670, L117

- Frail, D. A. 2011, *Mem. Soc. Astron. Italiana*, 82, 703
- Frail, D. A., Goss, W. M., Reynoso, E. M., et al. 1996, *AJ*, 111, 1651
- Gillessen, S., Eisenhauer, F., Fritz, T. K., et al. 2009, *ApJ*, 707, L114
- Goss, W. M., Schwarz, U. J., van Gorkom, J. H., & Ekers, R. D. 1985, *MNRAS*, 215, 69P
- Graham, J. R., Wright, G. S., & Longmore, A. J. 1990, *ApJ*, 352, 172
- Green, D. A. 2014, *Bulletin of the Astronomical Society of India*, 42, 47
- Green, A. J., Frail, D. A., Goss, W. M., & Otrupcek, R. 1997, *AJ*, 114, 2058
- Hatchell, J., Thompson, M. A., Millar, T. J., & MacDonald, G. H. 1998, *A&AS*, 133, 29
- Heard, V., & Warwick, R. S. 2013, *MNRAS*, 434, 1339
- Herrnstein, R. M., & Ho, P. T. P. 2005, *ApJ*, 620, 287
- Jiang, B., Chen, Y., Wang, J., et al. 2010, *ApJ*, 712, 1147
- Kalenskii, S. V., Dzura, A. M., Booth, R. S., Winnberg, A., & Alakoz, A. V. 1997, *A&A*, 321, 311
- Kalenskii, S. V., Promyslov, V. G., Slysh, V. I., Bergman, P., & Winnberg, A. 2006, *Astronomy Reports*, 50, 289
- Kalenskii, S. V., Johansson, L. E. B., Bergman, P., et al. 2010, *MNRAS*, 405, 613
- Kilpatrick, C. D., Biegging, J. H., & Rieke, G. H. 2014, *ApJ*, 796, 144
- Kilpatrick, C. D., Biegging, J. H., & Rieke, G. H. 2016, *ApJ*, 816, 1
- Koralesky, B., Frail, D. A., Goss, W. M., Claussen, M. J., & Green, A. J. 1998, *AJ*, 116, 1323
- Kuchar, T. A., & Clark, F. O. 1997, *ApJ*, 488, 224
- Leurini, S., Menten, K. M., & Walmsley, C. M. 2016, *A&A*, 592, A31
- Leurini, S., Schilke, P., Menten, K. M., et al. 2004, *A&A*, 422, 573
- Liechti, S., & Wilson, T. L. 1996, *A&A*, 314, 615
- Litovchenko, I. D., Alakoz, A. V., Val'Tts, I. E., & Larionov, G. M. 2011, *Astronomy Reports*, 55, 978
- Livio, M. 2000, *Unsolved Problems in Stellar Evolution*,
- Maeda, Y., Baganoff, F. K., Feigelson, E. D., et al. 2002, *ApJ*, 570, 671
- Mapelli, M., & Gualandris, A. 2016, *Lecture Notes in Physics*, Berlin Springer Verlag, 905, 205
- McEwen, B. C., Pihlström, Y. M., & Sjouwerman, L. O. 2014, *ApJ*, 793, 133
- Menten, K. M., Walmsley, C. M., Henkel, C., & Wilson, T. L. 1988, *A&A*, 198, 253
- Menten, K. M., Reid, M. J., Moran, J. M., et al. 1988, *ApJ*, 333, L83
- Mori, H., Tsuru, T. G., Hyodo, Y., Koyama, K., & Senda, A. 2008, *PASJ*, 60, 183
- Murray, C. D., & Dermott, S. F. 2000, *Solar System Dynamics*, by C.D. Murray and S.F. Dermott. ISBN 0521575974. Cambridge, UK: Cambridge University Press, 2000.
- Nesterenok, A. V. 2016, *MNRAS*, 455, 3978
- Paladini, R., Burigana, C., Davies, R. D., et al. 2003, *A&A*, 397, 213
- Penzias, A. A. & Burrus, C. A. 1973, *ARA&A*, 11, 51
- Pihlström, Y. M., Sjouwerman, L. O., & Fish, V. L. 2011, *ApJ*, 739, L21
- Pihlström, Y. M., Sjouwerman, L. O., Frail, D. A., et al. 2014, *AJ*, 147, 73
- Plambeck, R. L., & Menten, K. M. 1990, *ApJ*, 364, 555
- Ponti, G., Morris, M. R., Terrier, R., et al. 2015, *MNRAS*, 453, 172
- Predehl, P., & Schmitt, J. H. M. M. 1995, *A&A*, 293, 889
- Serabyn, E., Lacy, J. H., & Achtermann, J. M. 1992, *ApJ*, 395, 166
- Shan, W., Yang, J., Shi, S., et al. 2012, *IEEE Transactions on Terahertz Science and Technology*, 2, 593
- Sjouwerman, L. O., & Pihlström, Y. M. 2008, *ApJ*, 681, 1287
- Sjouwerman, L. O., & Pihlström, Y. M. 2012, *IAU Symposium*, 287, 449
- Sjouwerman, L. O., Pihlström, Y. M., & Fish, V. L. 2010, *ApJ*, 710, L111
- Slysh, V. I., Bachiller, R., Berulis, I. I., et al. 1994, *AZh*, 71, 37
- Sugizaki, M., Mitsuda, K., Kaneda, H., et al. 2001, *ApJS*, 134, 77
- Tsuboi, M., Miyazaki, A., & Okumura, S. K. 2009, *PASJ*, 61, 29
- Ulich, B. L. & Haas, R. W. 1976, *ApJS*, 30, 247
- Val'tts, I. E., Ellingsen, S. P., Slysh, V. I., et al. 2000, *MNRAS*, 317, 315
- Vink, J. 2012, *A&A Rev.*, 20, 49
- Wallace, B. J., Landecker, T. L., Kalberla, P. M. W., & Taylor, A. R. 1999, *ApJS*, 124, 181

- Wallace, B. J., Landecker, T. L., & Taylor, A. R. 1994, *A&A*, 286, 565
- Yang, W., Xu, Y., Chen, X., et al. 2017, arXiv:1705.01806
- Yusef-Zadeh, F., Cotton, W., Viti, S., Wardle, M., & Royster, M. 2013, *ApJ*, 764, L19
- Yusef-Zadeh, F., Goss, W. M., Roberts, D. A., Robinson, B., & Frail, D. A. 1999, *ApJ*, 527, 172
- Yusef-Zadeh, F., Hewitt, J. W., & Cotton, W. 2004, *ApJS*, 155, 421
- Yusef-Zadeh, F., Law, C., & Wardle, M. 2002A, *ApJ*, 568, L121
- Yusef-Zadeh, F., Law, C., Wardle, M., et al. 2002B, *ApJ*, 570, 665
- Yusef-Zadeh, F., Wardle, M., Rho, J., & Sakano, M. 2003, *ApJ*, 585, 319
- Zubrin, S. Y., & Shulga, V. M. 2008, *Young Scientists 15th Proceedings*, 41